Supplementary Material

Pixelated Bayer Spectral Router Based on Sparse Meta-atom Array

Yifan Shao (邵逸凡), Rui Chen (陈瑞), Yubo Wang (王钰博), Shuhan Guo (郭姝含), Junjie Zhan (詹俊杰), Pankaj K. Choudhury, and Yungui Ma (马云贵)*

State Key Lab of Modern Optical Instrumentation, Centre for Optical and Electromagnetic Research, College of Optical Science and Engineering; International Research Center (Haining) for Advanced Photonics, Zhejiang University, Hangzhou, 310058, China

***Corresponding author's E-mail:** yungui@zju.edu.cn

Section S1. Optical constants of used materials

Figure S1 plots the optical constants of Si_3N_4 and SiO_2. The refractive index and extinction coefficient of Si_3N_4 are measured by an ellipsometer. The refractive index of SiO_2 is obtained from the data measured by Malitson in 1965.

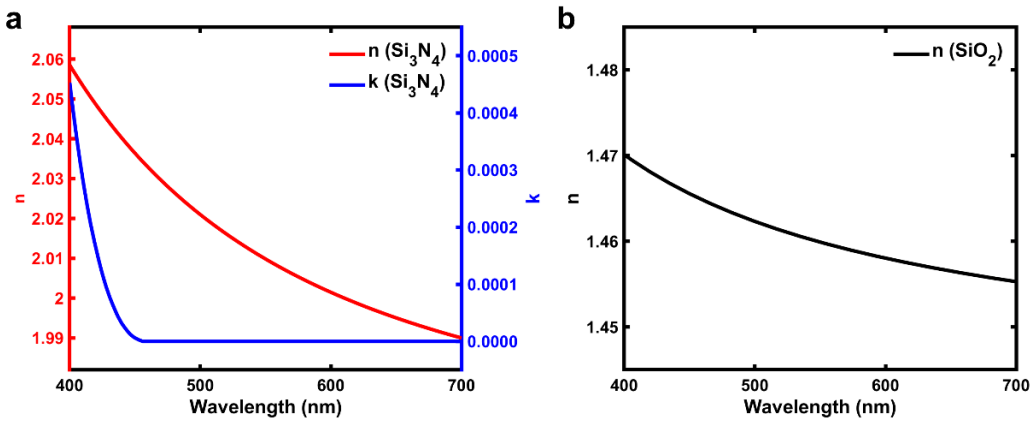

Fig. S1. (a) The refractive index and extinction coefficient of Si_3N_4. (b) The refractive index of SiO_2.

Section S2. Simulation method and optimization process of the Bayer spectral router

In this work, the full-wave electromagnetic simulation is executed by the commercial software Lumerical FDTD Solutions. We first model the supercell of the spectral router which includes four Si_3N_4 nanopillars on a SiO_2 substrate. The period of the supercell is 2.24 μm × 2.24 μm. Design parameters can be assigned to the model in real time to adjust structures during the optimization. The plane wave source is incident along the -Z direction. The periodic boundary condition is employed in both X and Y directions. The perfect matched layer (PML) boundary condition is employed in the Z direction. The mesh size of the simulation is set to 20 nm. Four frequency domain field and power monitors with a pixel size of 1.12 μm × 1.12 μm are arranged h_d away from the Si_3N_4 nanopillars to obtain the power flow distributions on the detecting plane, which can be used to evaluate the performance of the device and calculate the spectral routing efficiency.

The spectral routing efficiencies of R, G, and B channels as a function of wavelength are defined as

$$T_{\mathrm{R}}(\lambda) = \frac{\int_{\mathrm{R}} \mathrm{I}(x, y, \lambda)\, dxdy}{\int_{\mathrm{R+G_1+G_2+B}} \mathrm{I_i}(x, y, \lambda)\, dxdy} \tag{S1}$$

$$T_{\mathrm{G}}(\lambda) = \frac{\int_{\mathrm{G_1+G_2}} \mathrm{I}(x, y, \lambda)\, dxdy}{\int_{\mathrm{R+G_1+G_2+B}} \mathrm{I_i}(x, y, \lambda)\, dxdy} \tag{S2}$$

$$T_{\mathrm{B}}(\lambda) = \frac{\int_{\mathrm{B}} \mathrm{I}(x, y, \lambda)\, dxdy}{\int_{\mathrm{R+G_1+G_2+B}} \mathrm{I_i}(x, y, \lambda)\, dxdy} \tag{S3}$$

respectively, where $\mathrm{I}(x, y, \lambda)$ represents the intensity distribution on the detecting plane at the wavelength of λ, $\mathrm{I_i}(x, y, \lambda)$ represents the intensity distribution of incident light at the wavelength of λ, the subscripts of integral symbols indicate the pixel regions where the integral is performed. Figure S2(b) depicts the layout of R, G_1, G_2, and B pixels in the Bayer pattern.

The average spectral routing efficiencies of R, G, and B bands are defined as

$$\mathrm{Eff_R} = \frac{1}{\Delta\lambda_{\mathrm{R}}} \int_{600\ \mathrm{nm}}^{700\ \mathrm{nm}} T_{\mathrm{R}}(\lambda)\, d\lambda \tag{S4}$$

$$\mathrm{Eff_G} = \frac{1}{\Delta\lambda_{\mathrm{G}}} \int_{500\ \mathrm{nm}}^{600\ \mathrm{nm}} T_{\mathrm{G}}(\lambda)\, d\lambda \tag{S5}$$

$$\mathrm{Eff_B} = \frac{1}{\Delta\lambda_{\mathrm{B}}} \int_{400\ \mathrm{nm}}^{500\ \mathrm{nm}} T_{\mathrm{B}}(\lambda)\, d\lambda \tag{S6}$$

respectively, where $\Delta\lambda_{\mathrm{R}} = \Delta\lambda_{\mathrm{G}} = \Delta\lambda_{\mathrm{B}} = 100$ nm are bandwidths of R, G, and B bands.

Particle swarm optimization (PSO) algorithm is a robust stochastic evolutionary computation technique for finding the optimal solution in complex search spaces through the interaction of

individuals in a population of particles[1,2], which has long been applied in electromagnetics. In this work, we combine the PSO algorithm with FDTD simulation to find the optimal structure parameters for the spectral router. The figure of merit (FOM, i.e. fitness function) is set as

$$\mathrm{Eff} = \mathrm{Eff}_R + \mathrm{Eff}_G + \mathrm{Eff}_B \tag{S7}$$

which is the efficiency enhancement factor compared with the maximum efficiency of traditional Bayer image sensors with ideal color filters (100% transmittance in the passband). The FOM intends to obtain the highest possible spectral routing efficiency.

The number of solutions (particles) in each generation is set to 20, and the maximum generation number is set to 1000. First, the initial design parameters are randomly generated. Then, as shown in the optimization flow diagram in Fig. S2(a), in each iteration, numerical simulation of the spectral router is performed by Lumerical FDTD Solutions, followed by the calculation of FOM (fitness function). The criterion for optimization convergence is that the increase of FOM is less than 10^{-6} in 100 consecutive generations (i.e., 2000 solutions). The optimization is repeated until the convergence condition is met or the maximum number of generation is reached. Ultimately, the final design parameters are established for the fabrication of the spectral router.

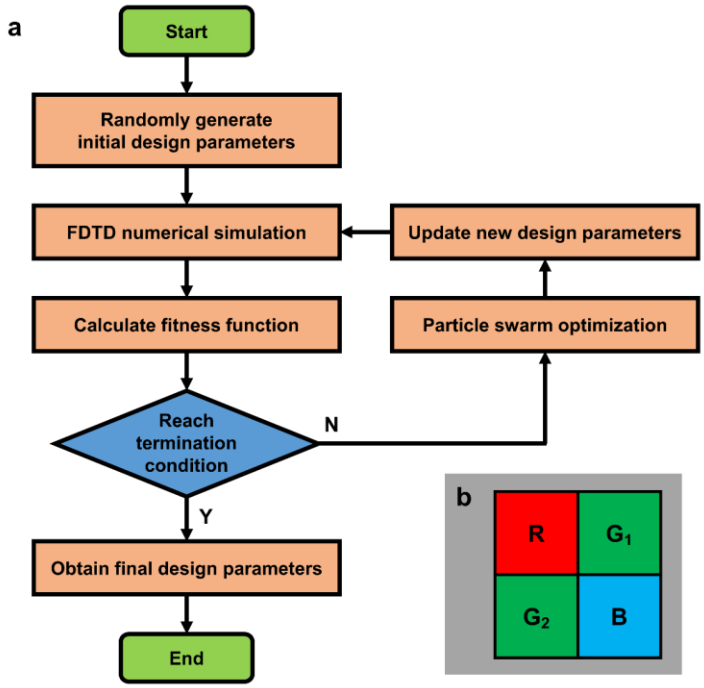

Fig. S2. (a) Optimization flow diagram of the pixelated spectral router. (b) Schematic top view of one supercell of the spectral router, corresponding to one Bayer cell (RGGB) of image sensor.

Section S3. The focusing effect for R, G, and B colors under limited aperture illumination

In order to demonstrate the working principle of sparse meta-atoms as dispersion-engineered micro-metalenses, Figure 2(a) in the main text shows the phase modulation profiles of one supercell for R, G, and B light, which are similar to those of ideal microlens array that meets the following phase distribution

$$\varphi_\lambda(x,y) = -\frac{2\pi}{\lambda}\left(\sqrt{f^2+(x-x_\lambda)^2+(y-y_\lambda)^2}-f\right)+C_\lambda \quad \text{(S8)}$$

especially for R and B light. In Equation S8, f is the focal length, x and y are coordinates of X-axis and Y-axis, (x_λ, y_λ) is the focus coordinate at the wavelength of λ, and C_λ is bias of the phase at the wavelength of λ. The phase modulation profile of G light deviates more from the ideal value, resulting in an inferior focusing effect compared to that of R and B light.

Figure S3 demonstrates the simulated focusing effect for R, G, and B color under limited aperture illumination, where the incident light only cover nine meta-atoms (regions enclosed by the white boxes in Figs. S3(a)-S3(c)). For R, G_2, and B pixels, respectively, corresponding nanopillars are arranged only on the central pixel and the eight surrounding pixels. R, G, and B arrows in Figs. S3(a)-S3(c) indicate the focusing direction of light. As shown in Figs. S3(d)-S3(i), the sparse meta-atoms function as a microlens, well focusing light towards the central pixel, thus making the central pixel collect energy that would otherwise be absorbed by color filters of the neighboring pixels of different colors. Note that for G light, the surrounding eight meta-atoms not only focus light towards the central G_2 pixel, but also route a portion of light to the four G_1 pixels in the four corners of the aperture. However, the four G_1 pixels in the four corners lack the light routed from adjacent pixels outside the white box in Fig. S3(b), which is indicated by the laurel-green dashed arrows in Fig. S3(b). Therefore, these four G_1 corners do not form perfect focal spots in this simulation. According to the above analysis, the contribution to the focusing effect primarily comes from the central meta-atoms and the neighboring meta-atoms on the pixels of colors different from the central pixel, indicating that the spatial crosstalk of the same color channel between supercells is small.

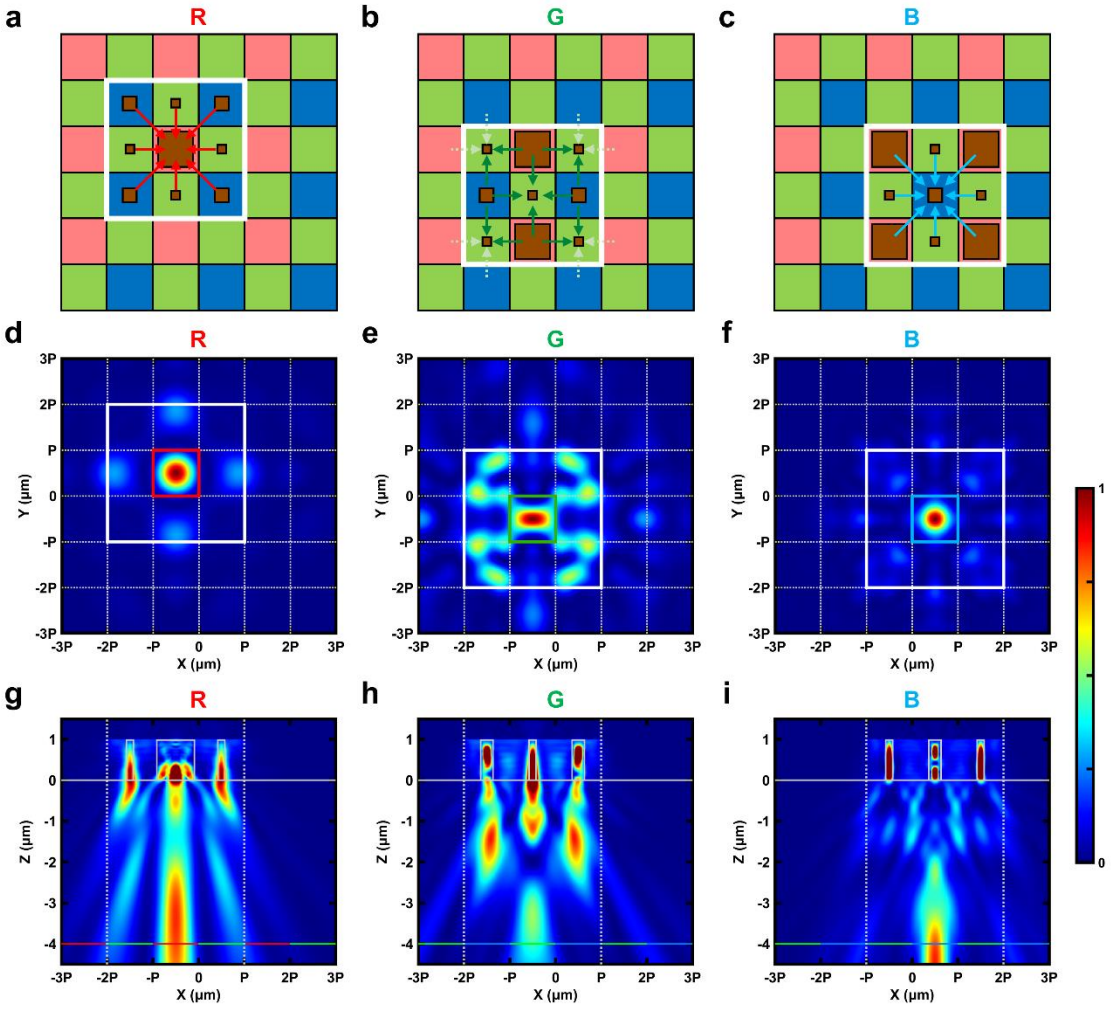

Fig. S3. The focusing effect for R, G, and B color under limited aperture illumination. (a)-(c) Schematics: For R, G_2, and B pixels, respectively, corresponding nanopillars are arranged only within the adjacent pixels. The white boxes indicate the aperture ranges of the incident light, covering nine meta-atoms. R, G, and B arrows indicate the focusing direction of light. (d)-(f) Power flow density distributions on the detecting plane at wavelengths of 650, 550, and 450 nm, respectively. The white boxes indicate the aperture ranges of incident light, covering nine pixels. (g)-(i) Power flow density distributions of the XZ cross section at wavelengths of 650, 550, and 450 nm, respectively. Gray rectangular boxes represent Si_3N_4 nanopillars. The R, G, and B solid lines at Z = -4 μm represent the detecting pixels of corresponding bands. The vertical dashed lines indicate the aperture ranges of incident light.

Section S4. Fabrication of the Bayer spectral router

The flow diagram of the sample processing is shown in Fig. S4. The quartz substrate is cleaned in the ultrasonic bath of acetone, isopropyl alcohol (IPA), and deionized water for 10 minutes, respectively. A Si_3N_4 film with a thickness of 998 nm is deposited on the substrate by PECVD. Then, a 170 nm thick positive electron-beam photoresist (ZEP520A) is spin-coated on the Si_3N_4 layer. The pattern of the device is written on the photoresist by EBL. After developing the photoresist, a 50 nm Cr layer is deposited by electron beam evaporation (EBE) and the Cr hard mask is patterned by the lift-off process. Finally, Si_3N_4 nanopillars are etched by RIE and the residual Cr mask is removed by inductively coupled plasma (ICP) etching.

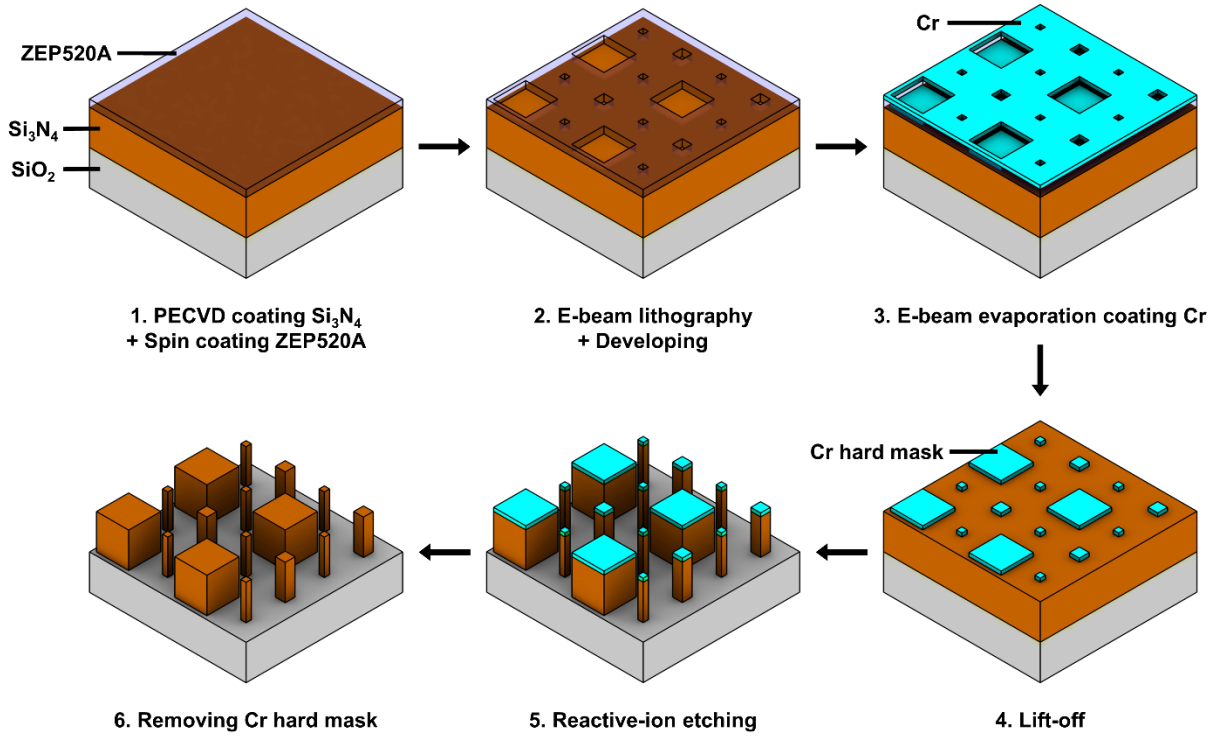

Fig. S4. Flow chart depicting the fabrication steps of the spectral router.

Section S5. Experimental characterizations of the Bayer spectral router

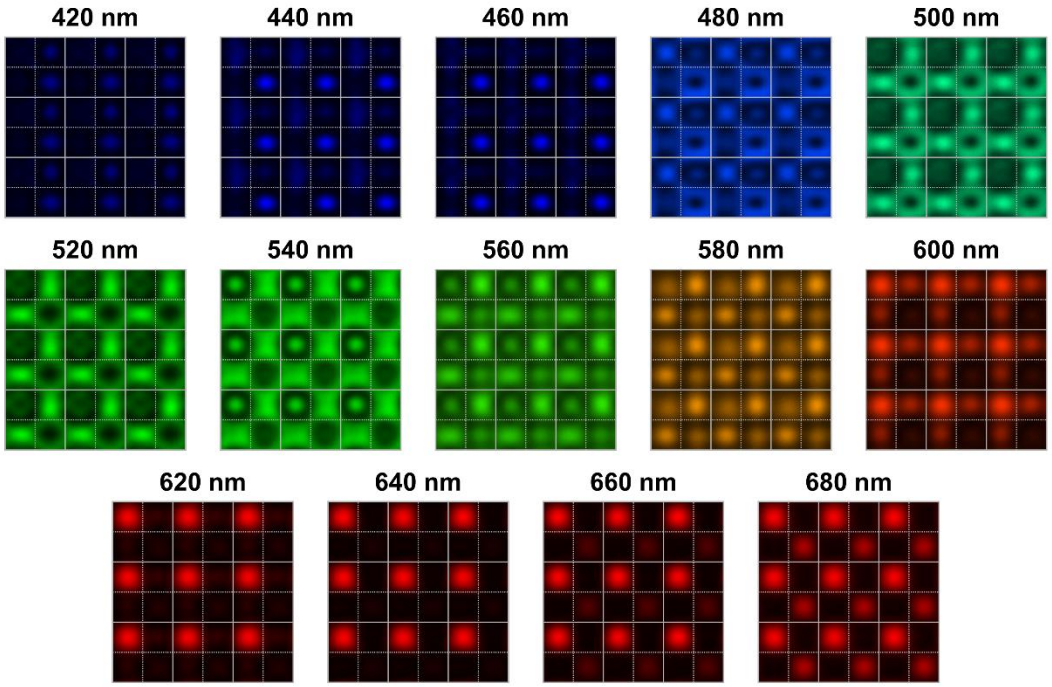

Fig. S5. Measured intensity profiles on the detecting plane of the spectral router at different wavelengths.

Section S6. Spectra of RGB bandpass color filters

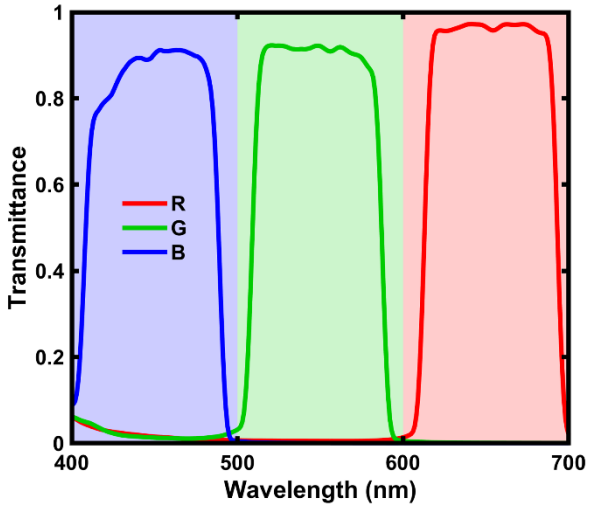

Fig. S6. Spectra of R, G, and B bandpass color filters used in the experiment of color imaging.

Section S7. Color imaging with the Bayer spectral router (Rubik's Cube)

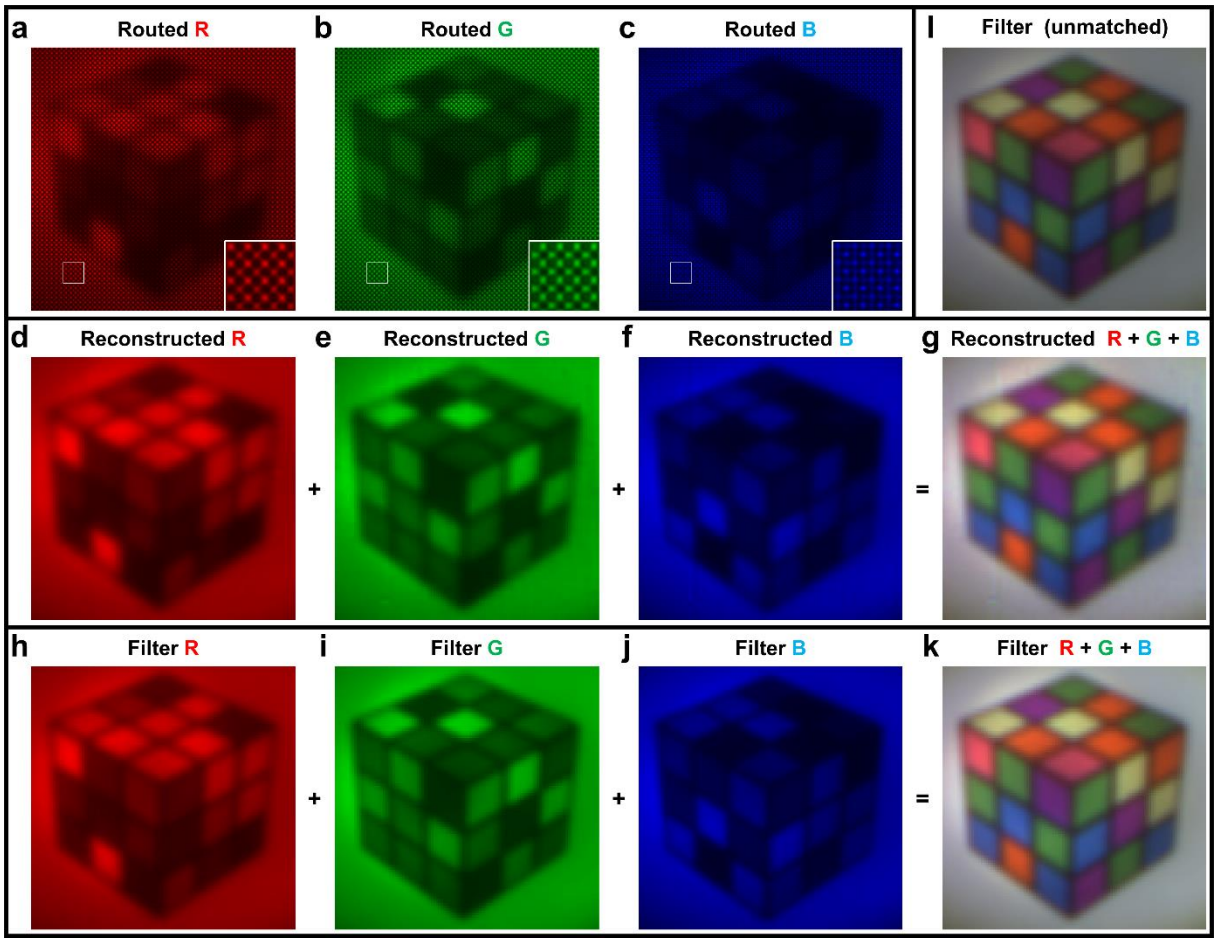

Fig. S7. Color imaging of the Rubik's Cube with the spectral router. (a)-(c) Measured intensity profiles of R, G, and B channels, respectively, on the detecting plane after the image is routed. (d)-(f) Reconstructed images of R, G, and B channels, respectively. (g) Reconstructed color image obtained from panels (d)-(f). (h)-(j) Reference images of R, G, and B channels obtained using only color filters without the spectral router. (k,l) Reference color image obtained from panels (h)-(j). Intensity of (k) is matched to that of (g).

The experimental setup for color imaging is shown in Fig. 4(a) of the main text. The object (Rubik's Cube) is placed 540 mm away from the imaging system and is imaged onto the spectral router. Figs. S7(a)-S7(c) present the measured intensity profiles on the detecting plane after the image is routed, which are obtained by inserting R, G, and B bandpass color filters, respectively. Then, the mosaic images of R, G, and B channels can be obtained directly according to the calibrated spectral routing efficiency. Figures S7(d)-S7(f) present the reconstructed images of R, G, and B channels, respectively, after demosaicing the images through bilinear interpolation.

Figures S7(h)-S7(j) present the reference images of R, G, and B channels obtained using the same experimental setup without the spectral router, which are also reconstructed by color correction and demosaicing. Figures S7(d)-S7(f) are in agreement with Figs. S7(h)-S7(j). Figures S7(g) and S7(k) are reconstructed color images with and without the spectral router after performing white balance, also showing a good agreement.

Section S8. Color imaging with the Bayer spectral router (ColorChecker)

We also performed the color imaging experiment on another object (ColorChecker) with the spectral router. The object (ColorChecker) is placed 665 mm away from the imaging system. The other experimental process and results are all analogous to Section S7.

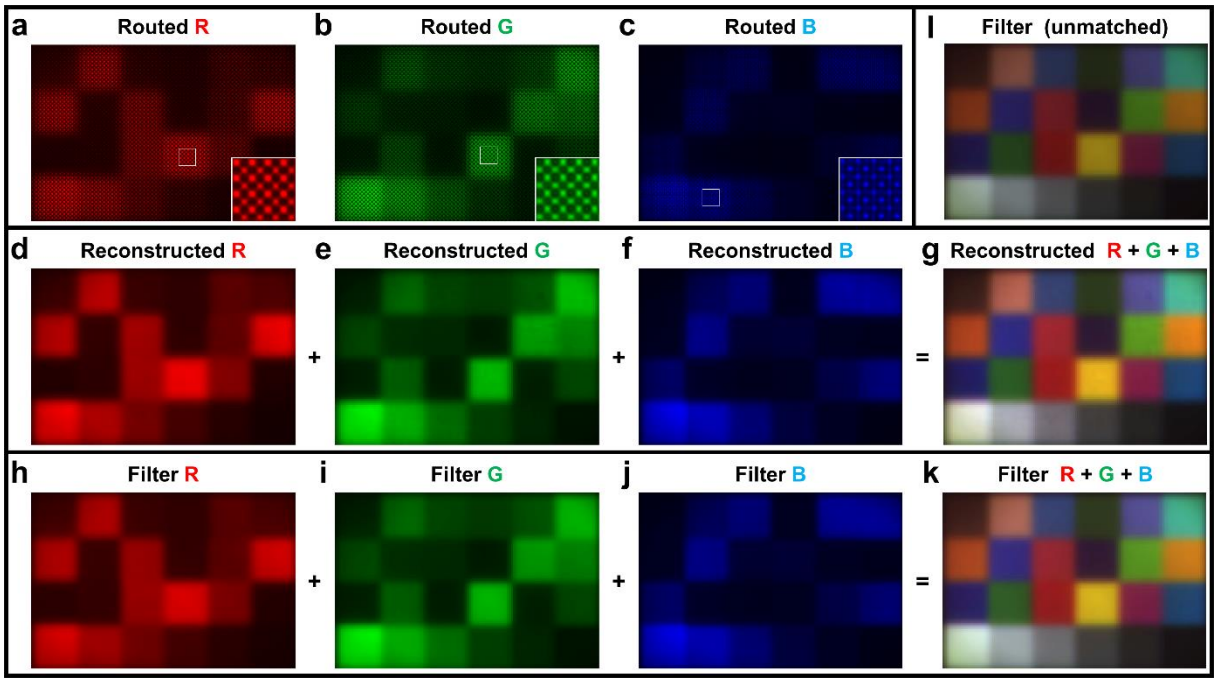

Fig. S8. Color imaging of the ColorChecker with the spectral router. (a)-(c) Measured intensity profiles of R, G, and B channels, respectively, on the detecting plane after the image is routed. (d)-(f) Reconstructed images of R, G, and B channels, respectively. (g) Reconstructed color image obtained from panels (d)-(f). (h)-(j) Reference images of R, G, and B channels obtained using only color filters without the spectral router. (k,l) Reference color image obtained from panels (h)-(j). Intensity of (k) is matched to that of (g).

Section S9. Efficiency enhancement for color imaging with the Bayer spectral router

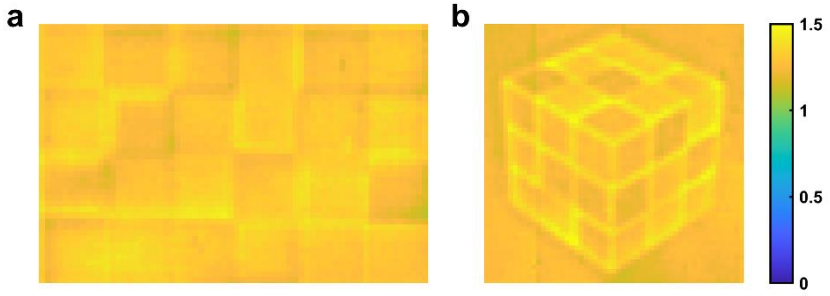

Fig. S9. Efficiency enhancement factor profile for color imaging with the Bayer spectral router. (a) ColorChecker, (b) Rubik's Cube.

Section S10. Polarization insensitivity of the Bayer spectral router

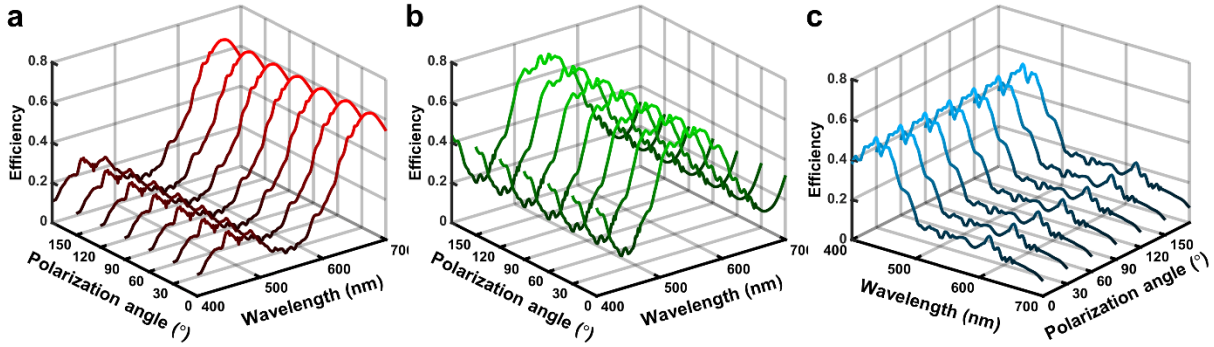

Fig. S10. Spectral routing efficiencies of (a) R, (b) G, and (c) B channels with different polarization angles.

Section S11. Incident angle tolerance, structure shift method and the specially optimized design under oblique incidence

Figure S11(c) plots simulated spectral routing efficiencies of R, G, and B channels under different incident angles. The average efficiency of R, G, and B channels remains higher than 33% up to a 10° incident angle. Some light intended to be routed to R/G_1/G_2/B pixels is misrouted to other pixels respectively due to the off-axis illumination, leading to the decreased spectral routing efficiency and anabatic crosstalk between channels. As shown in Fig. S11(a), the device efficiency under oblique incidence can be improved by shifting nanostructures according to the chief ray angle corresponding to pixel position. The arrows are just a view guidance for the diffraction of incident light. Under the incident angle of θ, the displacement of nanostructures is calculated by

$$\Delta x(\theta) = h \times \tan\left[\arcsin\left(\frac{\sin\theta}{n_{\text{eff}}}\right)\right] + h_{\text{d}} \times \tan\left[\arcsin\left(\frac{\sin\theta}{n_{\text{SiO}_2}}\right)\right], \quad \text{(S9)}$$

where n_{eff} is the effective refractive index of the nanostructure layer and n_{SiO_2} is the refractive index of SiO_2. The misrouted light can be transferred to the desired pixels by this method. For example, Figure S11(b) illustrates the simulated power flow density distributions of R, G, and B channels under 10° incidence, exhibiting the improved performance by shifting structures (Δx = 626 nm).

As shown in Fig. S11(d), by employing the structure shift method, the spectral routing efficiencies of R, G, and B channels remain nearly constant when the incident angle increases to 10°. Figure S11(e) plots the efficiency enhancement factor as a function of the incident angle with and without shifting structures, with the black horizontal dashed line representing the efficiency enhancement factor of an ideal conventional Bayer filter array. It intuitively reflects the significant role of the structure shift method in improving efficiency under oblique incidence. In the case of no shifting, the efficiency enhancement factor increases instead when the incident angle is larger than 18.5° because the obliquely traveling photons have reached the pixels of corresponding bands of the next supercell. Figure S11(f) plots average spectral routing efficiencies of R, G, and B channels as a function of the incident angle when using the structure shift method. The purple and green horizontal dashed lines represent the maximum efficiencies of an ideal Bayer color filter array for R/B (25%) and G (50%), respectively. Simulation results reveal that the structure shift method can expand the maximum acceptable chief ray angle to over 30°, which is applicable to image sensors with large areas.

Moreover, the spectral routing efficiency under the illumination of large incident angles can even be further improved by specially optimizing the nanostructures while keeping the height of nanopillars and the position of detecting plane unchanged (h = 998 nm, h_{d} = 4 μm). In this way, spectral routing efficiency higher than that of traditional filtering scheme can still be achieved even under 30° oblique incidence. Figure S11(g) plots the spectral routing efficiency under 30° incidence with specially optimized parameters (w_1 = 792 nm, w_2 = 205 nm, w_3 = 150 nm, Δx = -200 nm).

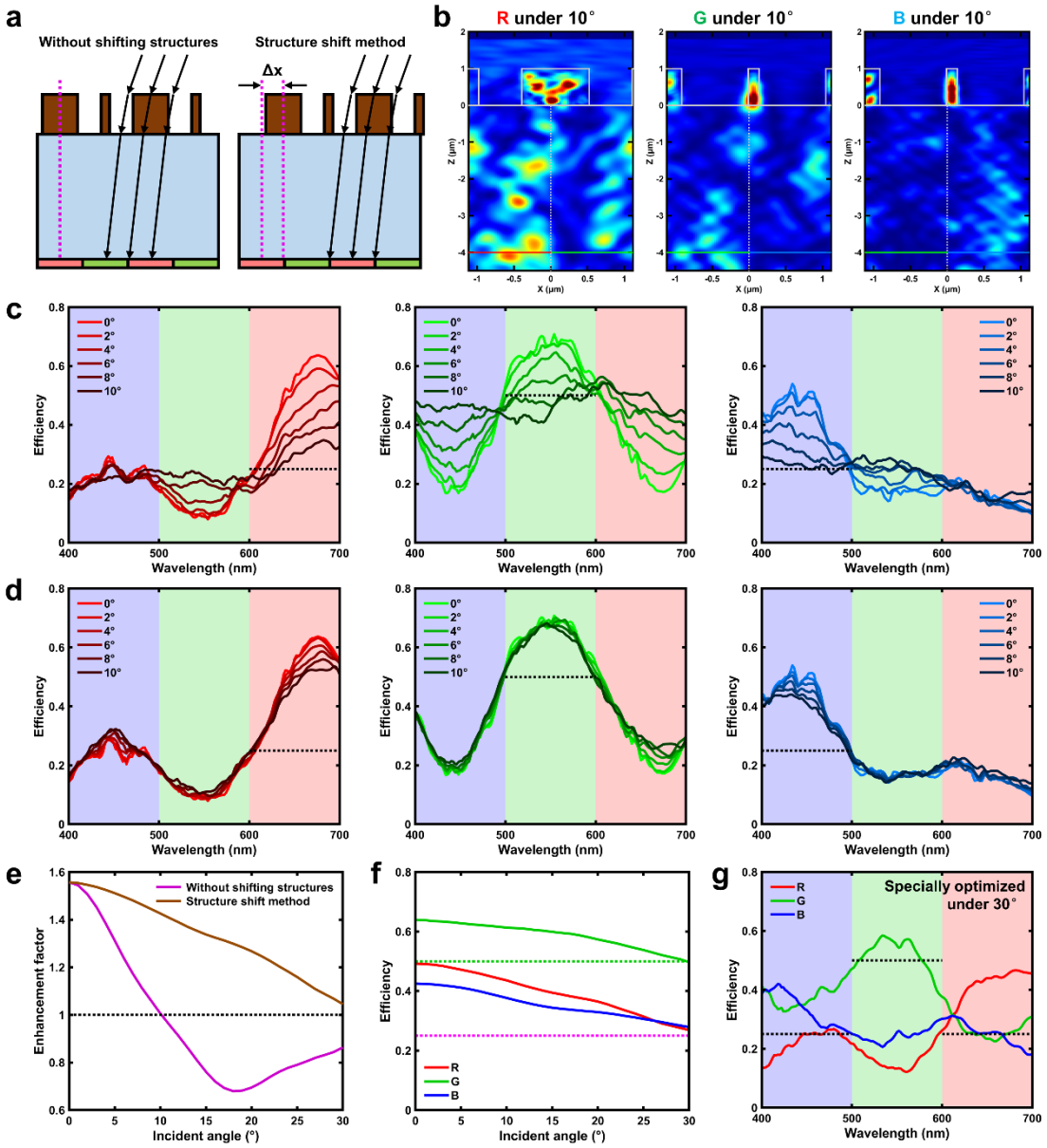

Fig. S11. (a) Schematics of the light propagation trajectory without and with the structure shift method. Δ*x* represents the shift length of structures. (b) Simulated power flow density distributions of the XZ cross section at wavelengths of 650, 550, and 450 nm under 10° incidence when using the structure shift method. Gray rectangular boxes represent Si_3N_4 nanopillars. (c) Simulated spectral routing efficiencies of R, G, and B channels under different incident angles without shifting structures. (d) Simulated spectral routing efficiencies of R, G, and B channels under different incident angles when using the structure shift method. (e) Efficiency enhancement factor as a function of the incident angle with and without shifting structures. (f) Average spectral routing efficiencies of R, G, and B channels as a function of the incident angle when using the structure shift method. (g) Simulated spectral routing efficiencies of R, G, and B channels under 30° incidence with specially optimized structures.

Section S12. Comparison between this work and previous spectral router

Some spectral routers were designed via single-layer code-like or freeform metasurfaces[3-6]. Figure S12(a) illustrates the layout of a Bayer spectral router based on code-like metasurfaces consisting of many fine nanostructures, which is like a chessboard[3]. Figure S12(b) illustrates the schematic top view of the Bayer spectral router designed in our work. The structural layout of our spectral router is very simple, with a relatively large feature size (150 nm) and all gaps between nanopillars larger than 500 nm, which is very promising for massive production. As shown in Figs. S12(c)-S12(e), the spectral router based on code-like metasurfaces exhibits high performance in the R and B channels, whereas the spectral routing efficiency of the G channel is about on par with that of the traditional color filter scheme. In this study, our spectral router notably improves the spectral routing efficiency of the G channel while maintaining the high performance of the R and B channels.

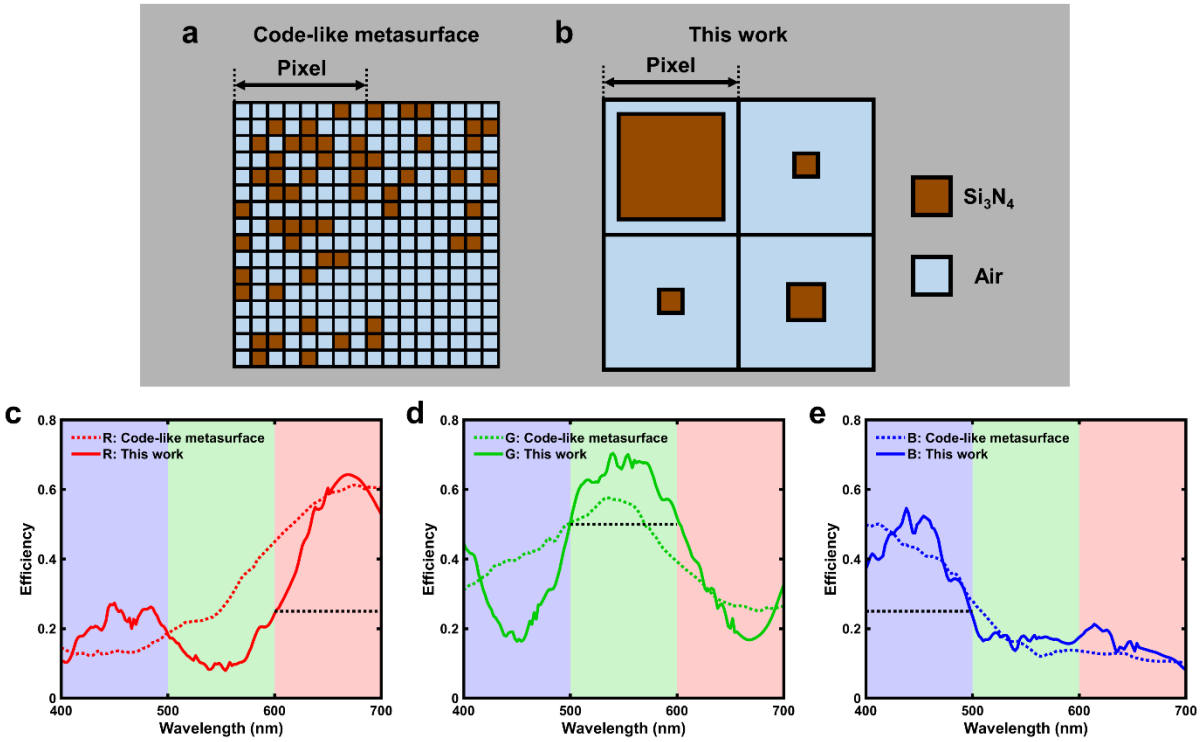

Fig. S12. (a) Structural layout of the spectral router based on code-like metasurfaces. (b) Structural layout of the spectral router in this work. (c)-(e) Comparison between efficiencies of spectral routers based on code-like metasurfaces and this work: spectral routing efficiencies of R, G, and B channels, respectively.

To intuitively demonstrate the advantages of our router, Table S1 compares the feature sizes, gaps between nanostructures, pixel sizes, and efficiency enhancement factors of this work with those of previous spectral routers. To avoid the influence of device fabrication errors and experimental measurement errors for a fair comparison, the efficiency enhancement factors are uniformly compared by the simulation design results. Compared to other spectral routers, our design can achieve similar or even higher efficiency while having the simpler structure layout, larger feature size and gaps between nanostructures. It is of great significance for massive production in practical industrial applications.

Table S1. Comparison between single-layer spectral routers

Reference	Scheme	Feature size	Gaps between nanosturctures	Pixel size	Efficiency enhancement factor (R + G + B)
Ref. [8]	Blazed grating	125 nm	190 nm	1.43 μm	(40-50%) × 3
Ref. [16]	Micro-metalens array	~80 nm	~100 nm	1.6 μm	65% + 50% + 25% = 1.4
Ref. [20]	Micro-metalens array	50 nm	~100 nm	25 μm	15.9% + 65.42% + 38.33% = 1.197*
Ref. [21]	Code-like metasurface	125 nm	125 nm	1 μm	~56.2% + 51.4% + 41.8% = 1.494
Ref. [23]	Code-like metasurface	100 nm	100 nm	1.1 μm	~ 49% + 49% + 42% = 1.4
Ref. [24]	Freeform metasurface	50 nm	~50 nm	0.6 μm	~52%+52%+56% = 1.6 60%+57%+65% = 1.82*
This work	Sparse meta-atoms	**150 nm**	**>500 nm**	1.12 μm	**51.13% + 62.91% + 42.57% = 1.566** **64.30% + 70.43% + 54.62% = 1.894***
		177 nm	**>250 nm**	**0.5 μm**	**55.35% + 65.88% + 41.65% = 1.629** **67.05% + 75.75% + 60.88% = 2.057***

Note: The reference numbers in Table S1 are corresponding to the reference numbers in the main text. All the efficiency enhancement factors are simulation design results to avoid the influence of device fabrication errors and experimental measurement errors. Asterisk * means the peak spectral routing efficiencies. The others are broadband average spectral routing efficiencies.

Section S13. Design of Bayer spectral routers for other pixel sizes

The supercell of the spectral router in the main text has a period of 2.24 μm ×2.24 μm, corresponding to one Bayer cell (RGGB) with the pixel size of 1.12 μm × 1.12 μm. In fact, our method of designing spectral routers based on sparse meta-atom array can be flexibly applicable to other pixel sizes. Here, we demonstrate Bayer spectral routers that are matched to pixel sizes of 1 μm × 1 μm and 0.5 μm × 0.5 μm, which are designed by the same structural layout in the main text.

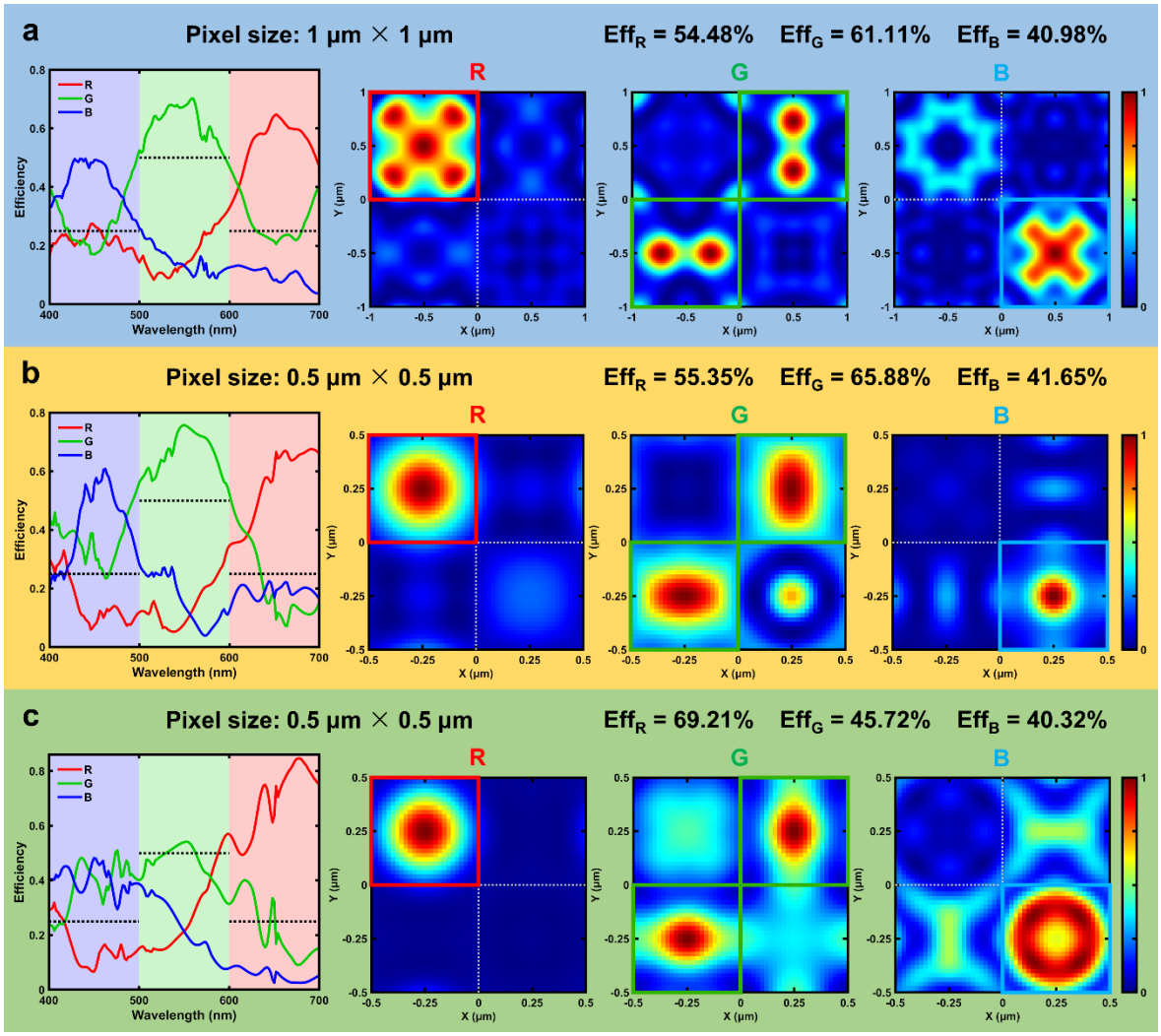

Fig. S13. Simulated spectral routing efficiencies and power flow density distributions on the detecting plane of three different designs. (a) 1 μm × 1 μm pixel size. (b) 0.5 μm × 0.5 μm pixel size, having a relatively balanced routing effect. (c) 0.5 μm × 0.5 μm pixel size, having high efficiency in the R channel but large crosstalk in the G and B channels.

(1) Design (a): Bayer spectral router matched to the pixel size of 1 μm × 1 μm

Parameters: w_1 = 928 nm, w_2 = 150 nm, w_3 = 276 nm, h = 986 nm, and h_d = 3 μm.

Average spectral routing efficiencies: $\mathrm{Eff_R}$ = 54.48%, $\mathrm{Eff_G}$ = 61.11%, $\mathrm{Eff_B}$ = 40.98%.

Figure S13(a) plots the simulated spectral routing efficiencies and power flow density distributions on the detecting plane of design (a).

(2) Design (b): Bayer spectral router matched to the pixel size of 0.5 μm × 0.5 μm

Parameters: w_1 = 293 nm, w_2 = 195 nm, w_3 = 276 nm, h = 1130 nm, and h_d = 3.05 μm.

Average spectral routing efficiencies: $\mathrm{Eff_R}$ = 55.35%, $\mathrm{Eff_G}$ = 65.88%, $\mathrm{Eff_B}$ = 41.65%.

Figure S13(b) plots the simulated spectral routing efficiencies and power flow density distributions on the detecting plane of design (b).

(3) Design (c): Bayer spectral router matched to the pixel size of 0.5 μm × 0.5 μm

Parameters: w_1 = 410 nm, w_2 = 174 nm, w_3 = 222 nm, h = 720 nm, and h_d = 2.48 μm.

Average spectral routing efficiencies: $\mathrm{Eff_R}$ = 69.21%, $\mathrm{Eff_G}$ = 45.72%, $\mathrm{Eff_B}$ = 40.32%.

Figure S13(c) plots the simulated spectral routing efficiencies and power flow density distributions on the detecting plane of design (c).

The efficiency enhancement factors of designs (a)-(c) are all higher than 1.55. Note that although the pixel sizes of designs (b) and (c) are both 0.5 μm × 0.5 μm, it is obvious that the efficiency of the R channel in design (c) is high, while the efficiencies of the G and B channels are low, resulting in serious crosstalk in these two channels. It is because the particle swarm optimization sometimes may get trapped in a locally optimal solution, resulting in a high figure of merit (FOM = $\mathrm{Eff_R}$ + $\mathrm{Eff_G}$ + $\mathrm{Eff_B}$) but with one of the ($\mathrm{Eff_R}$, $\mathrm{Eff_G}$, $\mathrm{Eff_B}$) being very high while the others being too low. To solve this issue, we employ the following FOM:

$$\mathrm{FOM} = \mathrm{Eff_R} + \mathrm{Eff_G} + \mathrm{Eff_B} - std\,(\mathrm{Eff_R},\ \mathrm{Eff_G},\ \mathrm{Eff_B}) \tag{S10}$$

where $std\,(\mathrm{Eff_R},\ \mathrm{Eff_G},\ \mathrm{Eff_B})$ is the standard deviation, which is added into FOM to make the optimized efficiencies of R, G, and B bands as close as possible. Through this method, as shown in design (b), we can achieve a balanced routing effect, ensuring high efficiencies for all R, G, and B channels, thus avoiding excessive crosstalk in any of the channels.

Section S14. Integration between the spectral router, color filter and photodetector array

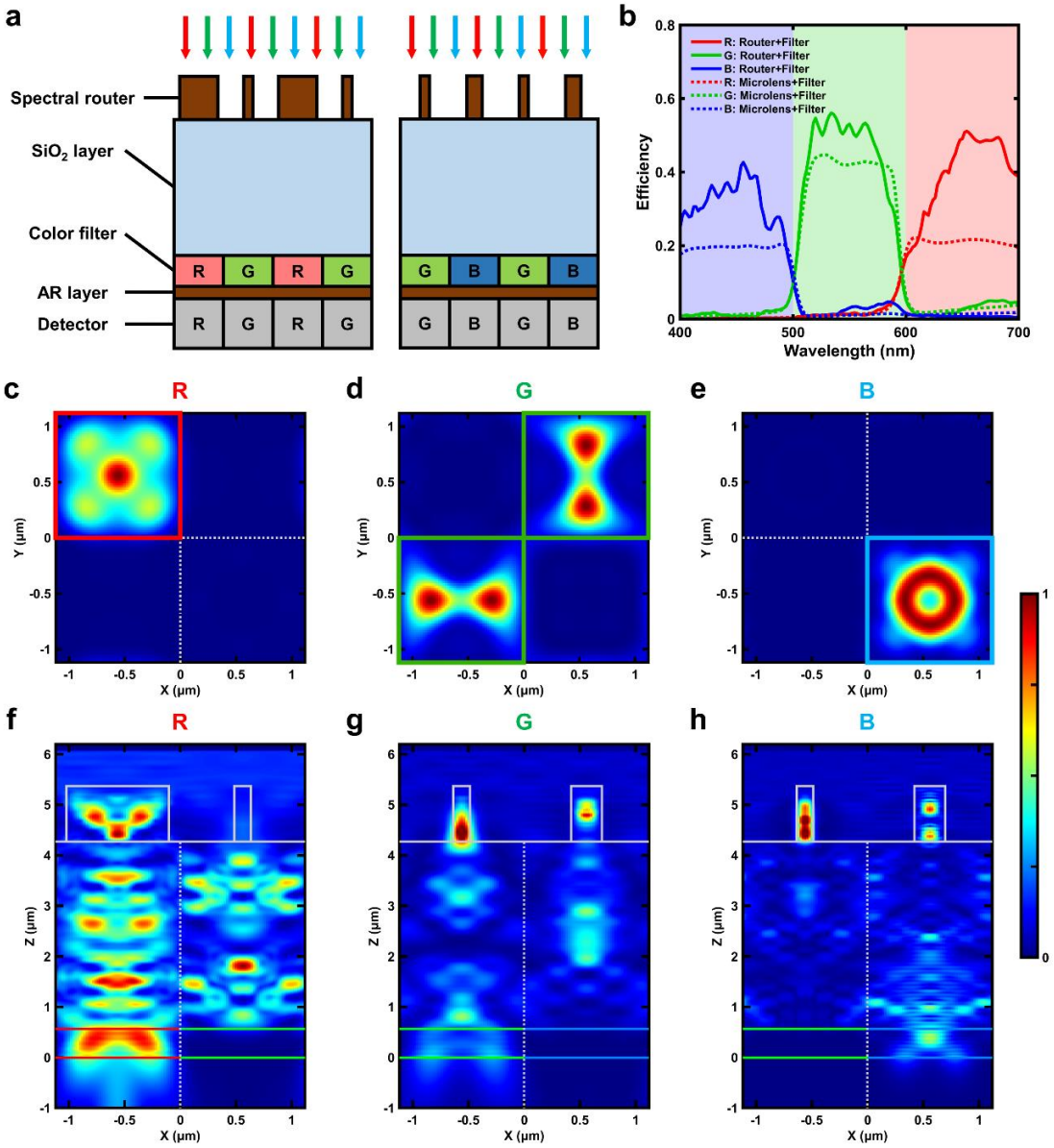

Fig. S14. (a) Schematic side view of the image sensor that integrates the spectral router, color filters, and photodetectors. (b) Comparison between efficiencies of combining the spectral router and color filters, and combining the microlens array and color filters (conventional image sensor). (c)-(e) Simulated power flow density distributions on the photodetectors after light passes through the spectral router and color filters at wavelengths of 650, 550, and 450 nm, respectively. (f)-(h) Simulated power flow density distributions of the XZ cross section at wavelengths of 650, 550, and 450 nm, respectively. Gray rectangular boxes represent Si_3N_4 nanopillars. Regions between two R/G/B solid lines represent corresponding color filters which can eliminate crosstalk.

Figure S14(a) illustrates the schematic side view of the image sensor that integrates the spectral router, color filters and silicon photodetectors. The thickness of color filters is set to 500 nm in the simulation [Z between 0 and 0.5 μm in Figs. S14(f)-S14(h)]. The refractive index of color filters is set to 1.5, and the extinction coefficient is set to 0.3 in the stopbands of color filters. The Si_3N_4 anti-reflection layer with a thickness of 70 nm can increase the transmittance. Figures S14(c)-S14(e) illustrate the power flow density distributions on the photodetectors at wavelengths of 650, 550, and 450 nm, respectively. Figures S14(f)-S14(h) illustrate the power flow density distributions in the propagation direction at wavelengths of 650, 550, and 450 nm, respectively. It is obvious that the crosstalk between different channels is significantly reduced by the color filter array. Figure S14(b) compares the simulated efficiencies between two architectures: (i) integrating the spectral router with color filters, and (ii) integrating the microlens array with color filters. It obviously reflects the significant role of spectral router in the efficiency enhancement.

Section S15. Impact of fabrication errors on device performance

In practical fabrication, there often exists slight processing errors, such as expansion and contraction of the widths of nanopillars, and errors in etching height. It has impact on the device performance. Figure S15 shows the effect of width and height errors on the efficiency of the spectral router. Figure S15(a) shows that both expansion and contraction of widths will lead to a decrease in the efficiency enhancement factor. As shown in Fig. S15(c), as the height increases, although the efficiencies of the R and B channels vary in opposite directions, the overall efficiency decreases slightly. However, it can be observed that $\pm$10% width errors and $\pm$100 nm height errors still ensure the efficiency enhancement factor > 1.4, which is much higher than that of traditional filtering scheme, indicating the design has good robustness.

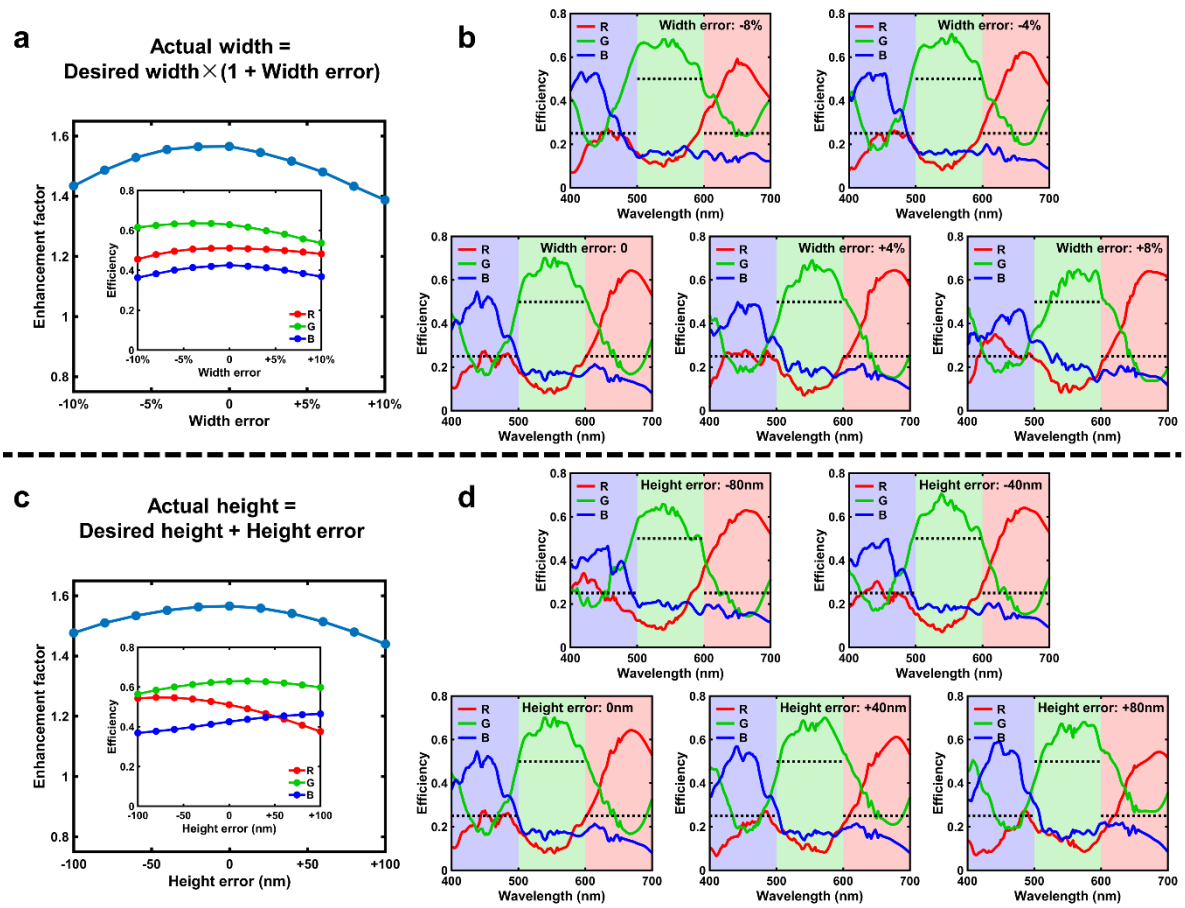

Fig. S15. Impact of fabrication errors on device performance. (a) Efficiency enhancement factor as a function of width error. The inset plots average spectral routing efficiencies Eff_R, Eff_G, and Eff_B as a function of width error. (b) Spectral routing efficiencies when width error = -8%, -4%, 0, 4%, and 8%, respectively. (c) Efficiency enhancement factor as a function of height error. The inset plots average spectral routing efficiencies Eff_R, Eff_G, and Eff_B as a function of width error. (d) Spectral routing efficiencies when height error = -80, -40, 0, 40, and 80 nm, respectively.

References

1. J. Kennedy and R. Eberhart, "Particle swarm optimization," in *International Conference on Neural Networks (ICNN)*, (1995), 1942.
2. M. Clerc and J. Kennedy, "The particle swarm - explosion, stability, and convergence in a multidimensional complex space," IEEE Transactions on Evolutionary Computation **6,** 58 (2002).

3. X. Zou, Y. Zhang, R. Lin*, et al.*, "Pixel-level Bayer-type colour router based on metasurfaces," Nature Communications **13,** 3288 (2022).
4. J. Li, Q. Zhang, H. Yang*, et al.*, "Single-layer Bayer metasurface via inverse design," ACS Photonics **9,** 2607 (2022).
5. M. Chen, L. Wen, D. Pan*, et al.*, "Full-color nanorouter for high-resolution imaging," Nanoscale **13,** 13024 (2021).
6. C. Kim, J. Hong, J. Jang*, et al.*, "Freeform metasurface color router for deep submicron pixel image sensors," Science Advances **10,** eadn9000 (2024).